Cationic Copper Species Stabilized by Zinc during the Electrocatalytic Reduction of CO_2 Revealed by In Situ X-Ray Spectroscopy

Juan-Jesús Velasco-Vélez,* Jeffrey Poon, Dunfeng Gao, Cheng-Hao Chuang, Arno Bergmann, Travis E. Jones, Shu-Chih Haw, Jin-Ming Chen, Emilia Carbonio, Rik V. Mom, Danail Ivanov, Rosa Arrigo, Beatriz Roldan Cuenya, Axel Knop-Gericke, and Robert Schlögl

Advanced in situ X-ray absorption spectroscopy characterization of electrochemically co-electrodeposited bi-element copper alloy electrodes shows that zinc yields the formation of a stable cationic Cu species during the electroreduction of CO_2 at high cathodic polarization. In contrast, the formation/stabilization of cationic Cu species in copper oxides, or doping Cu with another element, like Ni, is not possible. It is found that the pure and mixed Cu:Zn electrodes behave similarly in term of electrocatalytic selectivity to multi-carbon products. At higher Zn concentrations the electrode behaves like the pure Zn catalyst, which indicates that the Cu cationic species do not have a significant influence on the selectivity to multi-carbon products. It is found that in the non-monotonically distribution of products is dominated in term of surface energy in which copper prefers the surface. Otherwise, this work highlights the importance of in situ characterization to uncover the mechanisms mediating the catalytic reactions in contrast to ex situ or post mortem analysis, which can be a source of misinterpretation.

1. Introduction

The electrocatalytic pathway for renewable energy conversion into valuable chemicals plays a pivotal role in the transition to an energetically sustainable society, with CO_2 and H_2O as the cornerstone molecules.[1,2] In this way, the electrochemical reduction of CO_2 to valuable hydrocarbons and oxygenated products is proposed to occur in multiple steps: the reduction of CO_2 to CO and its subsequent conversion into oxygenates and hydrocarbon products.[3,4] The efficiency of this process competes against the parasitic hydrogen evolution reaction (HER) during the cathodic CO_2 reduction reaction (CO_2RR). The ideal CO_2 reduction should selectively yield only valuable multi-carbon products, which are

J.-J. Velasco-Vélez, A. Knop-Gericke, R. Schlögl
Department of Heterogeneous Reactions
Max Planck Institute for Chemical Energy Conversion
45470 Mülheim an der Ruhr, Germany
E-mail: jvelasco@cells.es

J.-J. Velasco-Vélez, T. E. Jones, R. V. Mom, D. Ivanov, A. Knop-Gericke, R. Schlögl
Department of Inorganic Chemistry
Fritz-Haber-Institut der Max-Planck-Gesellschaft
14195 Berlin, Germany

J.-J. Velasco-Vélez
ALBA Synchrotron Light Source
Cerdanyola del Vallés, Barcelona 08290, Spain

J. Poon, D. Gao, A. Bergmann, B. R. Cuenya
Department of Interface Science
Fritz-Haber-Institute of the Max-Planck Society
14195 Berlin, Germany

D. Gao
State Key Laboratory of Catalysis
Dalian Institute of Chemical Physics
Chinese Academy of Sciences
Dalian 116023, China

C.-H. Chuang
Department of Physics
Tamkang University
New Taipei City 25137, Taiwan

T. E. Jones
Los Alamos National Laboratory
Los Alamos, NM 87545, USA

S.-C. Haw, J.-M. Chen
National Synchrotron Radiation Research Center
No. 101, Hsin Ann Rr., East District, Hsinchu 30076, Taiwan

**ADVANCED
SCIENCE NEWS**
www.advancedsciencenews.com

**ADVANCED
SUSTAINABLE
SYSTEMS**
www.advsustainsys.com

energy-dense and product precursors of fuels, rather the less profitable methane. Hence, it is vital to design highly selective and active catalysts to achieve this goal. Copper remains the only element capable of producing hydrocarbons from the electroreduction of CO_2 at significant rates. Meanwhile the selective formation of the C_{3+} products is scarce, as was probed by Hori and co-workers in their pioneer investigations.[5–8] At high overpotentials, bulk copper displays a high selectivity toward methane and single-carbon (C_1) products during aqueous cathodic CO_2RR. High multi-carbon product selectivity is still challenged by the competition with the HER and low-carbon product formation.[9] Recently, the selectivity toward multi-carbon products from CO_2RR has been significantly improved via various rational catalyst designs as well as efficient electrolyte and process engineering.[3,10] These strategies include: modifying the surface morphology,[11] space limiting effects,[12] controlling the initial oxidation state of copper electrochemically[13] and thermally,[14] plasma treatment,[15,16] surface pH dependence,[17] using different electrolyte cations,[18] gas diffusion electrodes and flow cells,[19–21] support effects,[22] alloying copper,[23] or doping copper with different elements.[24,25]

Currently there is no universal agreement on the active site of copper for selective multi-carbon products formation. For example, factors controlling the catalytic properties of copper through morphology/roughness/strains resulting from the existence of numerous grain boundaries at the interface has been proposed.[26–28] Other studies proposed that small amounts of dissolved oxygen heteroatoms in the near-surface of the copper catalyst controls the selectivity to the multi-carbon products formation.[29] Thus, cationic copper species ($Cu^{\delta+}$) are suggested to be the active site for multi-carbon product formation because it has a more suitable C–O binding energy than pure copper. Nevertheless, the oxygen remaining in the copper electrode is not stable in significant amounts during the CO_2RR, as was probed recently by in situ surface and bulk sensitive X-ray spectroscopy,[13,14] in situ X-ray diffraction[30] and with ^{18}O isotope labeled ex situ mass spectrometry.[31] These studies indicate that the concentration of "subsurface" oxygen is marginal during the CO_2RR. This fact opens the possibility to significantly improve the catalytic performance of the copper electrode if the outstanding catalytic properties of subsurface oxygen embedded in the metallic copper matrix can be imitated, i.e., by alloying copper with another stable heteroatom(s) (with transition metals) that mimic the role of subsurface oxygen in the near-surface of the catalyst.[32]

Different metals have diverse binding energies (and CO_2RR rates) to CO, which allow the catalytic performance to be tuned through different reaction pathways.[33] Investigations with different transition metals suggest that increasing the C–O binding energy lowers the CO_2RR faradaic efficiency (FE), where it was found that these metals can perform C–C coupling at modest rates:[34] Au, Ag and Zn bind to CO weakly, while Ni, Pt and Fe show strong bonding to CO. These results provide an avenue for the fabrication of doped metallic copper electrodes with controlled activity and selectivity.[24] The stability of these modifiers and their impact on the conductivity of the Cu matrix should therefore be studied. The optimal modifier should have the same effect as embedded dilute oxygen atoms in the copper matrix, while being stable under harsh cathodic reaction conditions. However, the doping of a pure copper electrode with heteroatoms may modify the properties of the electrocatalyst in a way different to a simple linear combination of its principal components, making it difficult to predict the resulting (electronic) structure of the electrode and the ensuing CO_2RR selectivity. Hence systematic in situ/operando experiments are required to reveal the nature of the active sites of these complex electrodes during the CO_2RR.

Here, we prepared a set of electrodeposited CuNi, CuZn on Au electrodes with different ratios of copper versus nickel or zinc. It is known that the use of Cu_2O-ZnO mixtures improves the selectivity to electroreduction of CO_2 to methanol,[35–37] Cu functionalized with Ni, aiming to decrease the reaction overpotential, results in beneficial energy efficiency,[38] however, the enhanced performance of these alloys is less clear. We found that doping copper with a diluted amount of zinc prompts the stabilization of cationic $Cu^{\delta+}$ species during CO_2RR, where the fraction of active-stable Cu(I) is indicated by $\delta+$ lying on average between 0 and +1 oxidation state. In contrast to the $Cu^{\delta+}$ species on pure copper/copper-oxide electrodes,[13,14,39] significant amounts of $Cu^{\delta+}$ are present in zinc doped copper under CO_2RR conditions as the in situ measurements prove. The presence of the $Cu^{\delta+}$ species in the electrode is expected to enhance the electrocatalytic selectivity to multi-carbon and oxygenated species, which would then exceed a linear combination of catalytic activity of the principal chemical elements (Cu and Zn). Such a synergistic effect is not expected for CuNi electrodes which should be dominated by HER. In order to reveal the electronic structure of the doped electrodes during the electrocatalytic reaction, we performed advance in situ electrode preparation and characterization by X-ray absorption spectroscopy (XAS) using the L_3-edges of the 3d metals (Ni, Cu, and Zn) in the soft X-ray energy regime.

2. Results

Figure 1 shows the faradaic efficiency of different products for the CuZn electrodes, measured at -1.8 V versus Ag/AgCl in CO_2-saturared 100 mM $KHCO_3$ electrolyte. It was found that pure electrodeposited copper electrodes yield H_2, CO, CH_4, C_2H_4 as the main gas-phase products, HCOOH, and oxygenates (alcohols, aldehydes, ketones)[40] as the main liquid-phase products, as respectively shown in Figure 1A,B. In situ XAS characterization in total fluorescence yield (TFY) mode indicates that the pure copper electrode is reduced to metallic copper during CO_2RR, as shown in **Figure 2**A (sets of spectra with varying applied potentials are shown in Figures S2–S4, Supporting Information). Note that in the hard X-ray regime it is possible to extract information related to the atomic local environment and oxidation state, but since the pre-edge of K-edge reflects the transition from an occupied 1s to an unoccupied 3d, the core-hole lifetime broadening smears out the features of the pre-peak of the spectrum. Meanwhile, this

E. Carbonio
Helmholtz-Zentrum Berlin für Materialien und Energie
14109 Berlin, Germany
R. Arrigo
School of Sciences
University of Salford
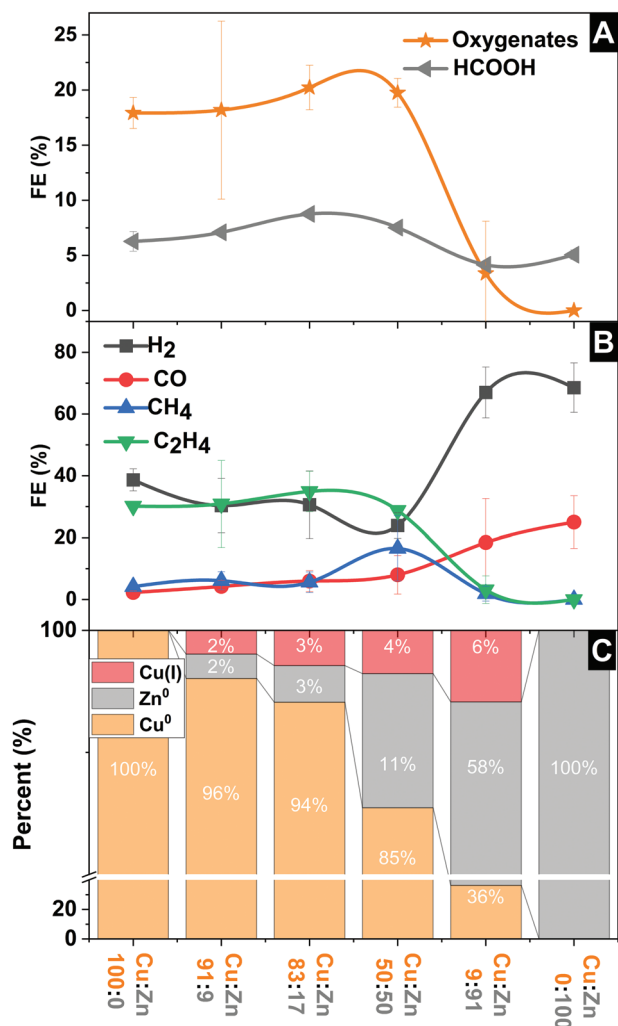Environment and Life, Cockcroft building, Manchester M5 4 WT, UK

**ADVANCED
SCIENCE NEWS**

www.advancedsciencenews.com

**ADVANCED
SUSTAINABLE
SYSTEMS**

www.advsustainsys.com

Figure 1. A) Liquid phase and B) gas phase products distribution of the CO_2RR reaction (in CO_2-saturated 100 mM $KHCO_3$ at −1.8 V versus Ag/AgCl) over copper electrodes with different ratios of zinc embedded atoms. C) Atomic fraction of each component calculated from the linear combination fitting (LCF) of the collected XA spectra during reaction conditions. The x axis represents the relative concentration of $CuSO_4$ versus $ZnSO_4$ electrolyte used for electrodeposited the electrodes on Au at −1.4 V versus Ag/AgCl.

products and formate produced over the CuZn samples were also found. For higher Zn concentrations the selectivity to hydrocarbon formation drops drastically at the same time that the H_2 and CO production are enhanced, following the trend found for pure Zn electrodes. The slight change in the FE of multi-carbon products indicates an insignificant impact of Zn on Cu in the formation of multi-carbon products.

In situ XAS experiments revealed that including 2% of Zn in the copper metallic lattice stabilizes up to 2% of Cu(I), estimated from a linear combination fitting (LCF) under reaction conditions (as shown in Figure 1C), which we denote $Cu^{0.02+}$. Increasing the concentration of Zn to 3% yields 3% stabilized Cu(I), $Cu^{0.03+}$, during CO_2RR conditions. Thus, $Cu^{0.03+}$ in the metallic copper electrode leads to a not significant effect on the FE to multi-carbons products compared to pure copper. Further increasing the zinc concentration in the copper (Zn:Cu $\geq$ 5) decreases the selectivity to multi-carbon products while simultaneously enhancing methane production and H_2, though the amount of $Cu^{\delta+}$ keeps increasing at higher Zn concentrations. Thus, the more Zn added, the higher the oxidation state of the whole copper electrode. The electrodes with lower concentration of Zn show higher multi-carbon selectivity than the electrodes with higher Zn concentration reported in the literature,[41] which likely operate similar to pure Zn electrodes. This trend is obvious because the electrodes dominated by the higher concentration of Zn likely have few copper atoms in close interaction with CO_2 and its performance is therefore dominated by the zinc, which tend to yield CO from the electroreduction of CO_2 rather than hydrocarbons and alcohols.

Unlike zinc-doped copper, co-electrodepositing copper with nickel results in increased hydrogen production, as shown in Figures S5 and S6 (Supporting Information). The in situ XAS-TFY measurements shown in Figure S7A (Supporting Information) reveal that in CuNi, the copper is fully reduced to metallic copper independent of the Ni concentration. In term of surface energies Cu should prefer the surface explaining the non-monotonically changes in the products distribution found. These experiments reveal that there is no formation of $Cu^{\delta+}$ in presence of Ni during the CO_2RR, indicating that the selection of the right doping element is key in stabilizing cationic copper to promote the selective production of multi-carbon species. More details of the in situ XAS-TFY measurements and products analysis for the CuNi electrodes can be found in the Supporting Information, including SEM (scanning electron microscopy) images of the electrodes in Figure S7 (Supporting Information).

3. Discussion

From the results above, it is clear that the insertion of Zn heteroatoms into the copper metallic lattice stabilizes $Cu^{\delta+}$ during CO_2RR conditions. It is thought that oxygen has similar effects on the formation of $Cu^{\delta+}$. However, oxygen is not stable under most of the cathodic polarization in a significant enough amount, including CO_2RR conditions, to be easily detectable.[13,14,39] In spite of this, before we discuss if the $Cu^{\delta+}$ species have any role on the enhanced selectivity-activity to the formation of multi-carbon products, the stabilization/formation mechanism of these species should be rationalized. In the literature, it was proposed that a small amount of ZnO coexist with metallic zinc
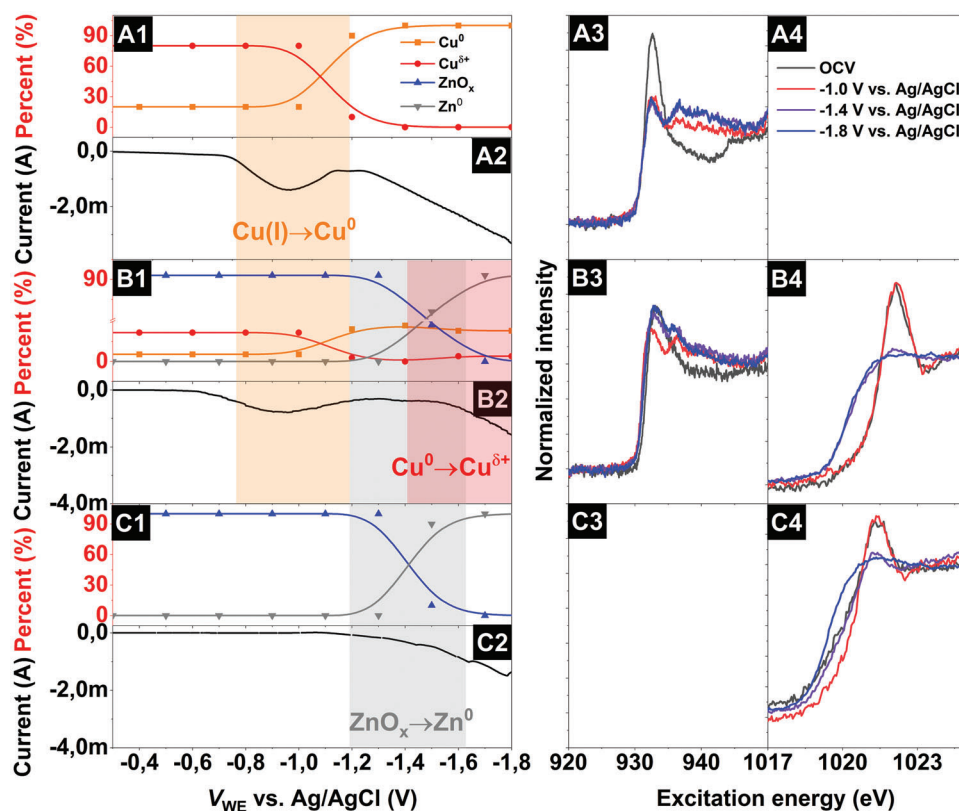
effect is less pronounced at the $L_{2,3}$-edges which probe the 2p→3d transitions that are less affected by lifetime broadening. Because of this fact, in this investigation we focused our experiments on the collection of the $L_{2,3}$-edges.

Unlike copper, pure zinc yields H_2 and CO gas-phase products together with HCOOH as a liquid-phase product, and the zinc electrode is reduced to Zn^0 during CO_2RR (see Figure 2C). The two pure electrodes are used as references indicating that pure copper has selectivity to multi-carbon products, while pure zinc does not. Thus, even in the absence of synergistic effects, changing the concentration of Cu versus Zn allows the catalytic selectivity to different products to be modified. Importantly, the ethylene faradaic efficiency reaches a maximum at around 35% for the CuZn sample, slightly higher than the 30% found for pure Cu. At the same time, moderated enhancement of the oxygenated

**ADVANCED
SCIENCE NEWS**

www.advancedsciencenews.com

**ADVANCED
SUSTAINABLE
SYSTEMS**

www.advsustainsys.com

Figure 2. Linear combination fitting (LCF), linear sweep voltammetry (LSV) in 100 mM $KHCO_3$ saturated in CO_2 and selected X-ray adsorption spectra (XAS) for A) pure copper, B) co-electrodeposited copper/zinc (sample 9:91), and C) pure zinc electrodes.

(Zn^0)[42–44] during the CO_2RR. However, our XAS experiments performed under reaction conditions suggest that the remaining species is $Cu^{\delta+}$ rather than $Zn^{\delta+}$, indicating a different mechanism than previously suggested. We probed the electronic structure of Cu an Zn using in situ XAS-TFY to observe changes in Cu and Zn $L_{2,3}$ edges as a function of the applied potential. Figure 2A shows the estimated LCF potential dependence of each copper species, as well as the linear sweep voltammograms (LSV) collected during the acquisition of the spectra. Figure 2A3 shows that pure copper reduces from Cu(I) to Cu^0 at around ≈1.0 V versus Ag/AgCl (highlighted in orange). Meanwhile, Figure 2C, shows that the reduction of pure zinc oxide to metallic Zn occurs at a more cathodic potential compared to pure copper, at around −1.4 V versus Ag/AgCl (highlighted in grey). It should be noticed that the reduction of copper and zinc electrodes occur at different potentials but both pure electrodes are reduced under CO_2RR conditions (−1.8 V vs Ag/AgCl) as shown by the XAS measurements.

The picture seen for pure electrodes differs significantly from the case of co-electrodeposited CuZn electrodes. Figure 2B1 shows the LCF estimated from the in situ XAS-TFY Cu and Zn L_3-edges with respect to the applied potential, as well as the LSV (Figure 2B2). Under these conditions, copper undergoes reduction at around −1.0 V versus Ag/AgCl (orange highlighted) and zinc is reduced at around −1.4 V versus Ag/AgCl (grey highlighted). Thus, there is no significant difference in the redox potential compared to the pure electrodes as shown in Figure 2A1,C1.

However, the reduction of Zn has a significant effect on the formation of $Cu^{\delta+}$ at cathodic potentials higher than −1.5 V versus Ag/AgCl, as shown in Figure 2B (red highlighted). This unique behavior can be explained by the $Cu^{\delta+}$ stabilization by the interaction of copper with zinc. This effect is clearly observed in the selected Cu and Zn L_3-edge XA spectra in Figure 2B3, B4, where the reduction of ZnO clearly prompts the formation of more $Cu^{\delta+}$ species. This is in good agreement with results seen in Cu-Zn nanoparticle systems.[45] In addition, these results highlight the importance of the in situ/operando experiments versus the ex situ characterizations, providing a clear description of the electronic structure changes observed under reaction conditions, which is not possible to conclude with ex situ or postmortem characterizations of these electrodes. The existence of small metallic clusters alloyed with Zn can also be responsible for the variation observed in the 3d-band.[46] In order to prove that the number of unoccupied 3d orbitals in copper is influenced by the inclusion of Zn atoms, calculations of the Cu L_3-edge with different amount of Zn were accomplished. Thus, the formation of the cationic copper species is yielded by the formation of the CuZn alloy as shown in **Figure 3**A measurements. This is corroborated, by the comparison of the measurements with the calculated spectra (shown in Figure 3B) for different amount of Zn incorporated in copper, i.e., Cu_4, Cu_7Zn and Cu_3Zn (as shown in Figure 3C). The comparison of these measurements and calculations clearly indicates that the changes in the number of emptied 3d orbitals in copper is ruled by the inclusion of
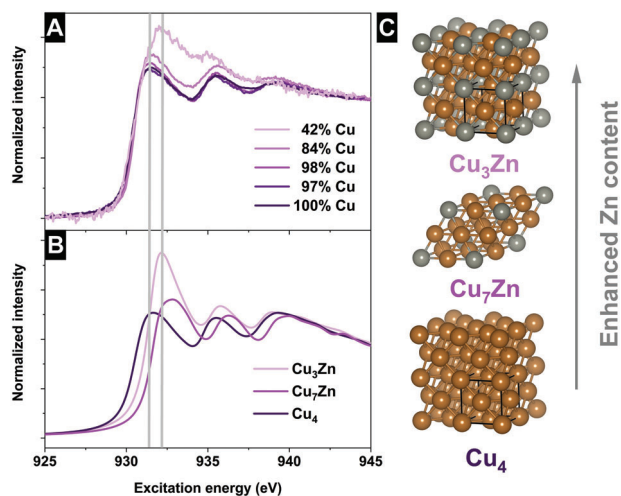
**ADVANCED
SCIENCE NEWS**

www.advancedsciencenews.com

**ADVANCED
SUSTAINABLE
SYSTEMS**

www.advsustainsys.com

Figure 3. A) Cu L_3-edge of CuZn electrodes collected under CO_2RR conditions with the Cu content indicated. B) Calculated spectra for Cu_4, Cu_3Zn, and Cu_7Zn. C) Ball and sticks models used for the spectra calculations.

Figure 4. Schema of the catalytic performance for an increased concentration of zinc versus copper.

Zn yielding enhanced presence of $Cu^{\delta+}$ species. Calculations details are shown in the Supporting Information. Thus, our experiments and calculations show that the addition of zinc to a copper electrode is accompanied by an enhancement $Cu^{\delta+}$ species during the CO_2RR, with no significant increase to the formation of multi-carbon products.

The effects that the addition of Zn does not have a significant influence on the catalytic activity beyond that the pure elements. Pure zinc electrodes evolve mostly CO as carbonaceous product, due to the weak interaction[47] of Zn with $CO^{\delta-}$. Thus, the CO leaves the Zn surface rather than form other products, consistent with a low adsorption strength. Meanwhile, copper yields the formation of multi-carbon and oxygenated products. It is expected that Zn in Cu lowers the dimerization energy barrier, which is the key step in the formation of the C–C bond[48] being promoted by the formation of $Cu^{\delta+}$ species.[49–51] The $Cu^{\delta+}$–CO bond strength is enhanced, thereby shifting the product selectivity path from a single-carbon to multi-carbon products. However, according to the results presented here, it is obvious that adding Zn to Cu does not have a significant impact on the catalytic activity and selectivity to the multi-carbon formation, thus the catalyst leans toward the pure Zn product yields where no influence of the $Cu^{\delta+}$ was identified. Thus, in the case of pure copper, the C–C bond formation is possible meanwhile in presence of Zn, CO, and H_2 formation is the dominant reaction pathway. Doping copper with other heteroatoms like Ni does not have any significant effect on the formation of more active $Cu^{\delta+}$ sites essential to enhance the catalytic activity, rather, Ni doping yields H_2 as main product of the reaction.

As explanation, of the non-monotonically changes in the products distribution found in this work, is related to the fact that copper prefer the surface respect zinc in term of surface energy, because the zinc surface energy is lower. This fact is shown schematically in **Figure 4**, which represents an increase of zinc versus copper on the right direction. Thus, the surface of the CuZn catalyst is dominated by the presence of copper until the concentration is two high and only few atoms of copper are
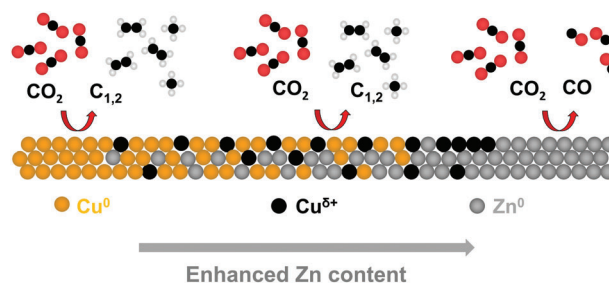
present. Under, enhanced zinc surface (with almost pure zinc electrodes) the reaction path way is dominated by the formation of CO and H_2. This effect explains the non-monotonically change in the selectivity to $C_{1,2}$ to CO and H_2 as consequence of surface energy.

4. Conclusion

In conclusion, our results provide clear evidence that doping a copper metal lattice with embedded heteroatoms of Zn does not significantly increase the activity/selectivity to the formation of valuable multi-carbon species, even the formation of $Cu^{\delta+}$ species during the CO_2RR was found in presence Zn. Thus, $Cu^{\delta+}$ species have no significant influence of these species in the reaction pathway. Furthermore, the non-monotonically changes in the selectivity from $C1_2$ to CO and H_2 is controlled by the surface energy of copper and zinc yielding a preference for copper in the surface, which in last term prompts the $C_{1,2}$ versus the CO/H_2 path way. Furthermore, the importance of the in situ/operando techniques to identify active species and reaction mechanism not accessible to ex situ characterizations is also highlighted in this work.

5. Experimental Section

Electrode Fabrication: The pristine Si_3N_4 membranes (type NX10100C) were sourced from Norcada (Edmonton, Canada). This membrane was semi-transparent to the incoming X-rays and separated the electrolyte from the vacuum chamber where the photo-detector was located. On the Si_3N_4 membrane (100 nm thick) a thin film of Cr (3 nm) adherence layer was deposited by physical vapor deposition (PVD). After that, 20 nm of Au were deposited onto the 3 nm Cr by PVD. A homogeneous polycrystalline thin film with an X-ray transmission through this membrane of ≈80% of the incoming intensity in the Ni, Cu, and $L_{2,3}$ edges range. This electrode was used for the co-electrodeposition of the different CuZn electrodes at −1.4 V versus Ag/AgCl using the next electrolytes bubbled with pure N_2 gas for eliminated the dissolved gases:

i) 5 mM $CuSO_4$ (100:0)
ii) 50 mM $CuSO_4$ + 5 mM $ZnSO_4$ (91:9)
iii) 25 mM $CuSO_4$ + 5 mM $ZnSO_4$ (83:17)
iv) 5 mM $CuSO_4$ + 5 mM $ZnSO_4$ (50:50)
v) 5 mM $CuSO_4$ + 50 mM $ZnSO_4$ (9:91)
vi) 5 mM $ZnSO_4$ (0:100)

The CuNi electrodes were electrodeposited at -1.4 V versus Ag/AgCl using the listed electrolytes bobbled with pure N_2 gas for eliminated the dissolved gases:

i) 5 mM $CuSO_4$ (100:0)
ii) 100 mM $CuSO_4$ + 50 mM $NiSO_4$ (66:33)
iii) 50 mM $CuSO_4$ + 100 mM $NiSO_4$ (33:66)
iv) 5 mM $NiSO_4$ (0:100)

After the electrodeposition of copper, the cell was flushed with pure water and subsequently filled with 100 mM $KHCO_3$, which was prepared by diluting 10 g of $KHCO_3$ (Roth, 99%) in 1 L of Milli-Q water (18.2 MΩ) at room temperature and saturated with pure CO_2 by bubbling the electrolyte.

The scanning electron microscopy (SEM) images of the electrodes are shown in Figure S1 (Supporting Information). In order to describe the changes in the electronic structure of each electrode, in situ XAS was used, which avoids artifacts that may be associated with ex situ analysis of post-reaction samples.[31] Using these samples, the CO_2RR product distribution as a function of the relative concentration of Cu versus Zn and Cu versus Ni provides a deeper understanding of the role in the selectivity/activity trends induced by Ni and Zn.

In Situ Electrochemical Flow Cell for X-Ray Absorption Spectroscopy and Beamline: The in situ electrochemical cell was operated in the main chamber of the ISISS beamline in BESSY II (Berlin, Germany) with a background pressure of $\approx 10^{-7}$ mbar while the aqueous electrolyte circulated on the back side of a Si_3N_4 membrane, where the electrodeposited thin film electrode is placed. In the ISISS beamline, the photons were sourced from a bending magnet (D41) and a plane grating monochromator (PGM) yielding an energy range from 80 to 2000 eV (soft X-ray range), a flux of 6×10^{10} photons s^{-1} with 0.1 A ring current using a 111 µm slit and an 80 µm $\times$ 200 µm beamspot size. The effective area of the electrode was ≈ 1.5 cm^2, which is determined by the diameter of the O-ring (0.7 cm) used for sealing the electrochemical cell. The measurements were recorded at cff 1.4 to avoid overlapping contribution of second order Si K-edge (from the Si_3N_4 membrane) on the plateau before the pre-edge of the Cu $L_{2,3}$ edges. Note that, no beam effects were observed during consecutive scans of the Ni, Cu, and Zn L-edges region, ruling out detectable beam-damage in the copper electrodes. The covered Si_3N_4 membrane were used as working electrodes and X-ray windows at the same time that separated the electrolyte from the vacuum, where the photo-diode detector was placed (AXUV100 Opto Diode Corp). The X-ray transmission through the Si_3N_4 membrane was estimated to be $\approx 80\%$ of the incoming X-ray intensity at the Ni, Cu, and Zn L-edges excitation energies. The main body of the cell was made of polyether ether ketone (PEEK), which is an electrical insulator and is chemically inert to most of the aqueous electrolytes. The counter electrode was a Pt wire and the reference electrode was a Ag/AgCl FLEXREF, sourced from World precision Instruments (Florida, USA).

The in situ XAS experiments were technically challenging, requiring typically the use of an electrochemical cell based in a thin X-ray membrane window (Si_3N_4 100 nm thick). The window was transparent to the incoming X-rays and outgoing photons, and it separated the liquid electrolyte from the vacuum side where a photo-detector was located. More details of the electrochemical cell can be found in a previous work.[14] Different copper electrodes were prepared by co-electrodeposition of Cu with Ni and Zn and successively used for the electroreduction of CO_2. Using this approach, the Cu, Ni, and Zn $L_{2,3}$-edge spectra of the different co-electrodeposited CuNi, CuZn were collected, and pure electrodes (prepared by in situ electrodeposition[52–54]) depending on the applied potential, i.e., during CO_2RR conditions. Note that the homogeneity of the electrodes was probed by EDX mapping of the elements as shown in the Supporting Information. Furthermore, using in situ XAS, detailed information of the Cu(I)/Cu^0 species distribution can be attained. For the analysis of the Cu L_3-edge spectra, linear combination fitting (LCF) of the principal components was employed.[14] The details of the electrochemical measurements and faradaic efficiency estimation can be found in the Supporting Information.

CO_2 Electroreduction Products Measurements

CO_2 electroreduction measurements were carried out in a gas-tight glass H-cell separated by an anion exchange membrane (Selemion AMV, AGC Inc.). Both, working electrode and counter electrode compartments were filled with 40 mL 100 mM $KHCO_3$ (Honeywell, 99.95%) and purged continuously with CO_2 (99.995%, 20 mL min^{-1}). A $KHCO_3$ solution was prepared with ultrapure water and further pre-purified with Chelex 100 Resin (Bio-Rad, 100–200 mesh). Prior to the measurement, the electrolyte was bubbled with CO_2 for 30 min to remove oxygen and saturate the solution. A platinum gauze (MaTecK, 3600 mesh) was used as the counter electrode and a leak-free Ag/AgCl electrode (3.4 M KCl, Innovative Instruments, Inc.) as reference electrode. The electrodes were electrodeposited on a gold mesh (Alfa Aesar 40931 gauze 0.064 mm, 99.9% metal basis), following the procedure described above for the electrodes prepared on the Si_3N_4 membrane. These electrodes were used as the working electrode and were contacted with a clamp wrapped by Kapton tape to avoid unwanted reactions. The potentials were controlled with an Autolab potentiostat (PGSTAT 204). All samples in this work were measured at a fixed potential of -1.8 V versus Ag/AgCl. The gas products were analyzed by online gas chromatography (GC, Agilent 7890B) every 20 min. H_2 and hydrocarbons were separated by different columns (Molecular sieve 13X, HayeSep Q, and Carboxen-1010 PLOT) and quantified by a thermal conductivity detector (TCD) and flame ionization detector (FID). The formic acid was analyzed by high-performance liquid chromatography (HPLC, Shimadzu Prominence) equipped with a NUCLEOGEL SUGAR 810 column and a refractive index detector (RID). Ethanol and 1-propanol were analyzed by liquid GC (Shimadzu 2010 plus), equipped with fused silica capillary column and FID.

Supporting Information

Supporting Information is available from the Wiley Online Library or from the author.

Acknowledgements

Conflict of Interest

The authors declare no conflict of interest.

Data Availability Statement

The data that support the findings of this study are available from the corresponding author upon reasonable request.

[1] R. Schlögl, *ChemSusChem* **2010**, *3*, 209.

[2] R. Schlögl, *Angew. Chem., Int. Ed.* **2022**, *61*, e202007397.

[3] D. Gao, R. M. Arán-Ais, H. S. Jeon, B. Roldan Cuenya, *Nat. Catal.* **2019**, *2*, 198.

[4] Y. Y. Birdja, E. Pérez-Gallent, M. C. Figueiredo, A. J. Göttle, F. Calle-Vallejo, M. T. M. Koper, *Nat. Energy* **2019**, *4*, 732.

[5] Y. Hori, K. Kikuchi, S. Suzuki, *Chem. Lett.* **1985**, *14*, 1695.

[6] Y. Hori, K. Kikuchi, A. Murata, S. Suzuki, *Chem. Lett.* **1986**, *15*, 897.

[7] Y. Hori, A. Murata, R. Takahashi, *J. Chem. Soc., Faraday Trans.* **1989**, *85*, 2309.

[8] Y. Hori, I. Takahashi, O. Koga, N. Hoshi, *J. Phys. Chem. B* **2002**, *106*, 15.

[9] W. Z. Li, *ACS Symp. Ser.* **2010**, *1056*, 55.

[10] S. Nitopi, E. Bertheussen, S. B. Scott, X. Liu, A. K. Engstfeld, S. Horch, B. Seger, I. E. L. Stephens, K. Chan, C. Hahn, J. K. Nørskov, T. F. Jaramillo, Ib Chorkendorff, *Chem. Rev.* **2019**, *119*, 7610.

[11] D. Gao, I. Zegkinoglou, N. J. Divins, F. Scholten, I. Sinev, P. Grosse, B. Roldan Cuenya, *ACS Nano* **2017**, *11*, 4825.

[12] P.-P. Yang, X.-L. Zhang, F.-Y. Gao, Y.-R. Zheng, Z.-Z. Niu, X. Yu, R. Liu, Z.-Z. Wu, S. Qin, L.-P. Chi, Y. Duan, T. Ma, X.-S. Zheng, J.-F. Zhu, H.-J. Wang, M.-R. Gao, S.-H. Yu, *JACS* **2020**, *142*, 6400.

[13] J.-J. Velasco-Vélez, T. Jones, D. Gao, E. Carbonio, R. Arrigo, C.-J. Hsu, Y.-C. Huang, C.-L. Dong, J.-M. Chen, J.-F. Lee, P. Strasser, B. Roldan Cuenya, R. Schlögl, A. Knop-Gericke, C.-H. Chuang, *ACS Sustainable Chem. Eng.* **2018**, *7*, 1485.

[14] J.-J. Velasco-Vélez, C.-H. Chuang, D. Gao, Q. Zhu, D. Ivanov, H. S. Jeon, R. Arrigo, R. V. Mom, E. Stotz, H.-L. Wu, T. E. Jones, B. Roldan Cuenya, A. Knop-Gericke, R. Schlögl, *ACS Catal.* **2020**, *10*, 11510.

[15] H. Mistry, A. S. Varela, C. S. Bonifacio, I. Zegkinoglou, I. Sinev, Y.-W. Choi, K. Kisslinger, E. A. Stach, J. C. Yang, P. Strasser, B. R. Cuenya, *Nat. Commun.* **2016**, *7*, 12123.

[16] K. Jiang, Y. Huang, G. Zeng, F. M. Toma, W. A. Goddard, A. T. Bell, *ACS Energy Lett.* **2020**, *5*, 1206.

[17] K. J. P. Schouten, E. Pérez Gallent, M. T. M. Koper, *J. Electroanal. Chem.* **2014**, *716*, 53.

[18] D. Gao, I. T. Mccrum, S. Deo, Y.-W. Choi, F. Scholten, W. Wan, J. G. Chen, M. J. Janik, B. Roldan Cuenya, *ACS Catal.* **2018**, *8*, 10012.

[19] C.-T. Dinh, T. Burdyny, Md. G. Kibria, A. Seifitokaldani, C. M. Gabardo, F. P García De Arquer, A. Kiani, J. P. Edwards, P. De Luna, O. S. Bushuyev, C. Zou, R. Quintero-Bermudez, Y. Pang, D. Sinton, E. H. Sargent, *Science* **2018**, *360*, 783.

[20] T. Möller, W. Ju, A. Bagger, X. Wang, F. Luo, T. Ngo Thanh, A. S. Varela, J. Rossmeisl, P. Strasser, *Environ. Sci.* **2019**, *12*, 640.

[21] P. Wei, H. Li, L. Lin, D. Gao, X. Zhang, H. Gong, G. Qing, R. Cai, G. Wang, X. Bao, *Sci. China: Chem.* **2020**, *63*, 1711.

[22] Z. Q. Liang, T. T. Zhuang, A. Seifitokaldani, J. Li, C. W. Huang, C. S. Tan, Y. Li, P. De Luna, C. T. Dinh, Y. Hu, Q. Xiao, P.-L. Hsieh, Y. Wang, F. Li, R. Quintero-Bermudez, Y. Zhou, P. Chen, Y. Pang, S.-C. Lo, L.-J. Chen, H. Tan, Z. Xu, S. Zhao, D. Sinton, E. H. Sargent, *Nat. Commun.* **2018**, *9*, 3828.

[23] E. L. Clark, C. Hahn, T. F. Jaramillo, A. T. Bell, *JACS* **2017**, *139*, 15848.

[24] Y. Zhou, F. Che, M. Liu, C. Zou, Z. Liang, P. De Luna, H. Yuan, J. Li, Z. Wang, H. Xie, H. Li, P. Chen, E. Bladt, R. Quintero-Bermudez, T.-K. Sham, S. Bals, J. Hofkens, D. Sinton, G. Chen, E. H. Sargent, *Nat. Chem.* **2018**, *10*, 974.

[25] D. Gao, I. Sinev, F. Scholten, R. M. Arán-Ais, N. J. Divins, K. Kvashnina, J. Timoshenko, B. Roldan Cuenya, *Angew. Chem., Int. Ed.* **2019**, *58*, 17047.

[26] R. Kas, R. Kortlever, A. Milbrat, M. T. M. Koper, G. Mul, J. Baltrusaitis, *Phys. Chem. Chem. Phys.* **2014**, *16*, 12194.

[27] C. W. Li, M. W. Kanan, *J. Am. Chem. Soc.* **2012**, *134*, 7231.

[28] A. Verdaguer-Casadevall, C. W. Li, T. P. Johansson, S B. Scott, J. T. Mckeown, M. Kumar, I E. L. Stephens, M. W. Kanan, Ib Chorkendorff, *J. Am. Chem. Soc.* **2015**, *137*, 9808.

[29] A. Eilert, F. Cavalca, F S Roberts, J. Osterwalder, C. Liu, M. Favaro, E. J. Crumlin, H. Ogasawara, D. Friebel, L. G. M. Pettersson, A. Nilsson, *J. Phys. Chem. Lett.* **2017**, *8*, 285.

[30] S. B. Scott, T. V. Hogg, A. T. Landers, T. Maagaard, E. Bertheussen, J. C. Lin, R. C. Davis, J. W. Beeman, D. Higgins, W. S. Drisdell, C. Hahn, A. Mehta, B. Seger, T. F. Jaramillo, Ib Chorkendorff, *ACS Energy Lett.* **2019**, *4*, 803.

[31] Y. Lum, J. W. Ager, *Angew. Chem., Int. Ed.* **2018**, *57*, 551.

[32] T.-C. Chou, C.-C. Chang, H.-L. Yu, W.-Y. Yu, C.-L. Dong, J.-J. Velasco-Vélez, C.-H. Chuang, L.-C. Chen, J.-F. Lee, J.-M. Chen, H.-L. Wu, *J. Am. Chem. Soc.* **2020**, *142*, 2857.

[33] Y. Katayama, F. Nattino, L. Giordano, J. Hwang, R. R. Rao, O. Andreussi, N. Marzari, Y. Shao-Horn, *J. Phys. Chem. C* **2018**, *123*, 5951.

[34] K. P. Kuhl, T. Hatsukade, E. R. Cave, D. N. Abram, J. Kibsgaard, T. F. Jaramillo, *J. Am. Chem. Soc.* **2014**, *136*, 14107.

[35] J. Albo, A. Sáez, J. Solla-Gullón, V. Montiel, A. Irabien, *Appl. Catal., B* **2015**, *176–177*, 709.

[36] J. Albo, A. Irabien, *J. Catal.* **2016**, *343*, 232.

[37] J. Albo, G. Beobide, P. Castaño, A. Irabien, *J. CO2 Util.* **2017**, *18*, 164.

[38] I. Merino-Garcia, J. Albo, P. Krzywda, G. Mul, A. Irabien, *Catal. Today* **2020**, *346*, 34.

[39] J.-J. Velasco-Velez, R. V. Mom, L.-E. Sandoval-Diaz, L. J. Falling, C.-H. Chuang, D. Gao, T. E. Jones, Q. Zhu, R. Arrigo, B. Roldan Cuenya, A. Knop-Gericke, T. Lunkenbein, R. Schlögl, *ACS Energy Lett.* **2020**, *5*, 2106.

[40] Y. Lum, J. W. Ager, *Energy Environ. Sci.* **2018**, *11*, 2935.

[41] D. Ren, B. S.-H. Ang, B. S. Yeo, *ACS Catal.* **2016**, *6*, 8239.

[42] D. L. T. Nguyen, M. S. Jee, D. H. Won, H. Jung, H. -. S. Oh, B. K. Min, Y. J. Hwang, *ACS Sustainable Chem. Eng.* **2017**, *5*, 11377.

[43] H. S. Jeon, J. Timoshenko, F. Scholten, I. Sinev, A. Herzog, F. T. Haase, B. Roldan Cuenya, *J. Am. Chem. Soc.* **2019**, *141*, 19879.

[44] H. S. Jeon, I. Sinev, F. Scholten, N. J. Divins, I. Zegkinoglou, L. Pielsticker, B. R. Cuenya, *J. Am. Chem. Soc.* **2018**, *140*, 9383.

[45] J. Timoshenko, H. S. Jeon, I. Sinev, F. T. Haase, A. Herzog, B. Roldan Cuenya, *Chem. Sci.* **2020**, *11*, 3727.

[46] A. Longo, F. Giannici, M. P. Casaletto, M. Rovezzi, C J. Sahle, P. Glatzel, Y. Joly, A. Martorana, *ACS Catal.* **2022**, *12*, 3615.

[47] K. C. Waugh, *Catal. Today* **1992**, *15*, 51.

[48] Y. Zhang, Y. Zhao, C. Wang, Z. Wei, J. Yang, J. Ma, *Phys. Chem. Chem. Phys.* **2019**, *21*, 21341.

[49] F. Dattila, R. Garciá-Muelas, N. López, *ACS Energy Lett.* **2020**, *5*, 3176.

[50] C. Wei, R. Zhang, L. Ling, D. Li, B. Hou, B. Wang, *Chem. Eng. Sci.* **2020**, *224*, 115785.

[51] M. Favaro, H. Xiao, T. Cheng, W. A. Goddard, J. Yano, E J. Crumlin, *Proc. Natl. Acad. Sci. U. S. A.* **2017**, *114*, 6706.

[52] J.-J. Velasco-Vélez, K. Skorupska, E. Frei, Y.-C. Huang, C.-L. Dong, B.-J. Su, C.-J. Hsu, H.-Y. Chou, J.-M. Chen, P. Strasser, R. Schlögl, A. Knop-Gericke, C.-H. Chuang, *J. Phys. Chem. B* **2018**, *122*, 780.

[53] J. J. Velasco-Vélez, T. E. Jones, V. Pfeifer, C.-L. Dong, Y.-X. Chen, C.-M. Chen, H.-Y. Chen, Y.-R. Lu, J.-M. Chen, R. Schlögl, A. Knop-Gericke, C.-H. Chuang, *J. Phys. D: Appl. Phys.* **2016**, *50*, 024002.

[54] J. J. Velasco-Velez, V. Pfeifer, M. Hävecker, R. S. Weatherup, R. Arrigo, C.- H. Chuang, E. Stotz, G. Weinberg, M. Salmeron, R. Schlögl, A. Knop-Gericke, T. E. Jones, *Angew. Chem., Int. Ed.* **2015**, *54*, 14554.